Microporous and Mesoporous Materials 244 (2017) 109–118

Contents lists available at ScienceDirect

Microporous and Mesoporous Materials

journal homepage: www.elsevier.com/locate/micromeso

Natrolites with different Fe^{2+}/Fe^{3+} cation ratios

Yongmoon Lee [a], Thomas Vogt [b], Yongjae Lee [a, c, *]

[a] Center for High Pressure Science and Technology Advanced Research, Shanghai 201203, China
[b] NanoCenter and Chemistry Department, University of South Carolina, Columbia, SC 29208, USA
[c] Department of Earth System Sciences, Yonsei University, Seoul 03722, South Korea

HPSTAR 359-2017

ARTICLE INFO

Article history:
Received 25 October 2016
Received in revised form
16 February 2017
Accepted 17 February 2017
Available online 20 February 2017

Keywords:
Natrolite
Iron
High-pressure/high-temperature
Rietveld refinement

ABSTRACT

We report the synthesis and structural characterization of two iron-exchanged natrolites, $Fe^{2+}_{4.0}Fe^{3+}_{2.7}Al_{16}Si_{24}O_{80}\cdot 29(1)H_2O$ (Fe-NAT4951) and $Fe^{2+}_{6.4}Fe^{3+}_{1.1}Al_{16}Si_{24}O_{80}\cdot 24H_2O$ (Fe-NAT8119) at different pressures and temperatures using ambient, high-temperature and in-situ high-pressure synchrotron powder X-ray diffraction, Mössbauer spectroscopy and extended X-ray absorption fine structure (EXAFS). At ambient conditions, Fe-NAT4951 crystallizes in an orthorhombic structure with space group **F***dd2* whereas the structure of Fe-NAT8119 is monoclinic with **C***c* symmetry. Due to the presence of more H_2O molecules in Fe-NAT4951 the channels are more circular as indicated by a T_5O_{10} (T = Si,Al) chain rotation angle of 12.6(1)° compared to 20.4(1)° in Fe-NAT8119. The coordination number of the Fe^{2+} and Fe^{3+} cations in the channels of Fe-NAT4951 is 3 and 4, whereas Fe-NAT8119 has 7- and 4-fold coordination, respectively. The two materials behave differently under hydrostatic pressures: due to a discontinuous pressure-induced hydration the volume of Fe-NAT8119 expands by 14.1(1) % near 1.0(1) GPa, whereas the volume of Fe-NAT4951 gradually decreases with pressure. Under increasing temperature and as a result of abrupt dehydration, the unit cell volume of Fe-NAT4951 contracts by ca. 8.3(1) % near 125(1) °C whereas Fe-NAT8119 contracts only by ca. 5.0(1) % near 225(5) °C.

1. Introduction

Iron-containing zeolites, such as Fe-ZSM-5 or the beta polymorph A (BEA), have been studied for decades due to their catalytic activities promoting important chemical reactions such as oxidizing benzene to phenol, the selective oxidation of methane to methanol, NO_x reduction and N_2O decomposition [1–5]. In particular, the realization of an efficient process converting methane to methanol would have enormous economic implications [6]. All of these reactions are conjectured to be based on the redox capabilities of iron present as either an extra-framework cation (EFC) or iron-hydrogen clusters within the zeolite channels [7,8]. Inelastic neutron scattering on Fe-ZSM5 revealed two distinct adsorption sites involved in the chemisorption of molecular hydrogen at 110 K [3]. In certain microorganisms methane monooxygenase which has a bimetallic Fe_2O_2 active site can convert methane to methanol [9]. Based on mainly spectroscopic evidence it was suggested that iron species contained in zeolites assemble in a so-called α-Fe(II) center. Recent work by Snyder et al. [10] proposes an alternative structural arrangement where the zeolite environment imposes an unusual square-planar geometry for the mononuclear Fe(II) center which then transforms to a mononuclear Fe(IV) = O species as a reactive intermediate. Understanding how to substitute iron into zeolites and create 'entatic states' similar to what has been observed in metalloenzymes [11] is a promising route for the development of new heterogeneous catalysts.

Natrolite ($Na_{16}Al_{16}Si_{24}O_{80}\times 16H_2O$, **F***dd2*, V = 2250 Å^3) is one of the naturally occurring small pore zeolites. We recently reported on the substitution of various cations into natrolite, and their crystal structures at different pressures and temperatures [12–17]. The physical and chemical properties after pressure-induced insertion of H_2O [16–19], CO_2 [20], or noble gas atoms Ar [21], Kr and Xe [22] into natrolites derive from the complex interplay of extra-framework cations (EFCs) and H_2O molecules present in the pores. Here we report on the successful synthesis of two new iron exchanged-forms of natrolites with different ratios of Fe^{2+}/Fe^{3+} ratios and describe their structures at ambient and non-ambient conditions.

* Corresponding author. Department of Earth System Sciences, Yonsei University, Seoul 03722, South Korea.
E-mail address: yongjaelee@yonsei.ac.kr (Y. Lee).

http://dx.doi.org/10.1016/j.micromeso.2017.02.062
1387-1811/

2. Experimental methods

A Fe-natrolite with a 49:51% ratio of Fe^{2+} and Fe^{3+} (Fe-NAT4951) was prepared using 1 M $FeCl_2 \cdot 4H_2O$ (ACS reagent grade from Sigma-Aldrich) which was adjusted to a pH of 0.2 and a molarity of 0.01 M in a nitric acid solution. A ground K-natrolite [12] (K-NAT, $K_{15.5(2)}Al_{16}Si_{24}O_{80} \times 14.0(2)H_2O$) powder was then added to a solution with a 100:1 ratio of solute to powder weight, respectively. The mixture was stirred at 80 °C in a closed system minimizing water loss. After 24 h, the solid was separated from the solution by centrifugation. The dried powder was then subjected to two more such exchange cycles. The final product was washed with a nitric acid solution of pH 0.2 and 0.01 M, and subsequently air-dried at ambient conditions. The other Fe-natrolite with a ratio of 80:20% of Fe^{2+}/Fe^{3+} ratio (Fe-NAT8119) was prepared by mixing $FeCl_2 \cdot 4H_2O$ and K-NAT powder in a 10:1 wt ratio. This mixture was then sealed in a quartz ampule and heated at 140 °C for 48 h. The final product was again washed with a nitric acid solution of pH 0.2 and 0.01 M, and air-dried at ambient conditions. Chemical analyses on these two products were performed using energy-dispersive X-ray spectroscopy (EDS) and indicated a 92(1) % Fe-exchange for Fe-NAT4951 and a 98(1) % Fe-exchange for Fe-NAT8119. To determine the Fe^{2+}/Fe^{3+} ratio in the two Fe-NATs, we used Mössbauer spectroscopy. We observed overlapping signals of Fe^{2+} and Fe^{3+} after measuring each sample for a week as seen in Fig. 1b. The relative area of the two sites was then used to calculate a 49(1):51(1) % and 81(1):19(1) % ratio of Fe^{2+} and Fe^{3+} in Fe-NAT4951 and Fe-NAT8119, respectively. To determine the amount of H_2O molecules inside the channels we did thermogravimetric analysis (TA instruments, TGA2050) at the Korea Basic Science Institute in Seoul. We used a heating range of 25–1000 °C and a heating rate of 10 °C/min under a nitrogen atmosphere.

High-resolution synchrotron X-ray powder diffraction data of the Fe-NATs were measured at the 9B beam line of the Pohang

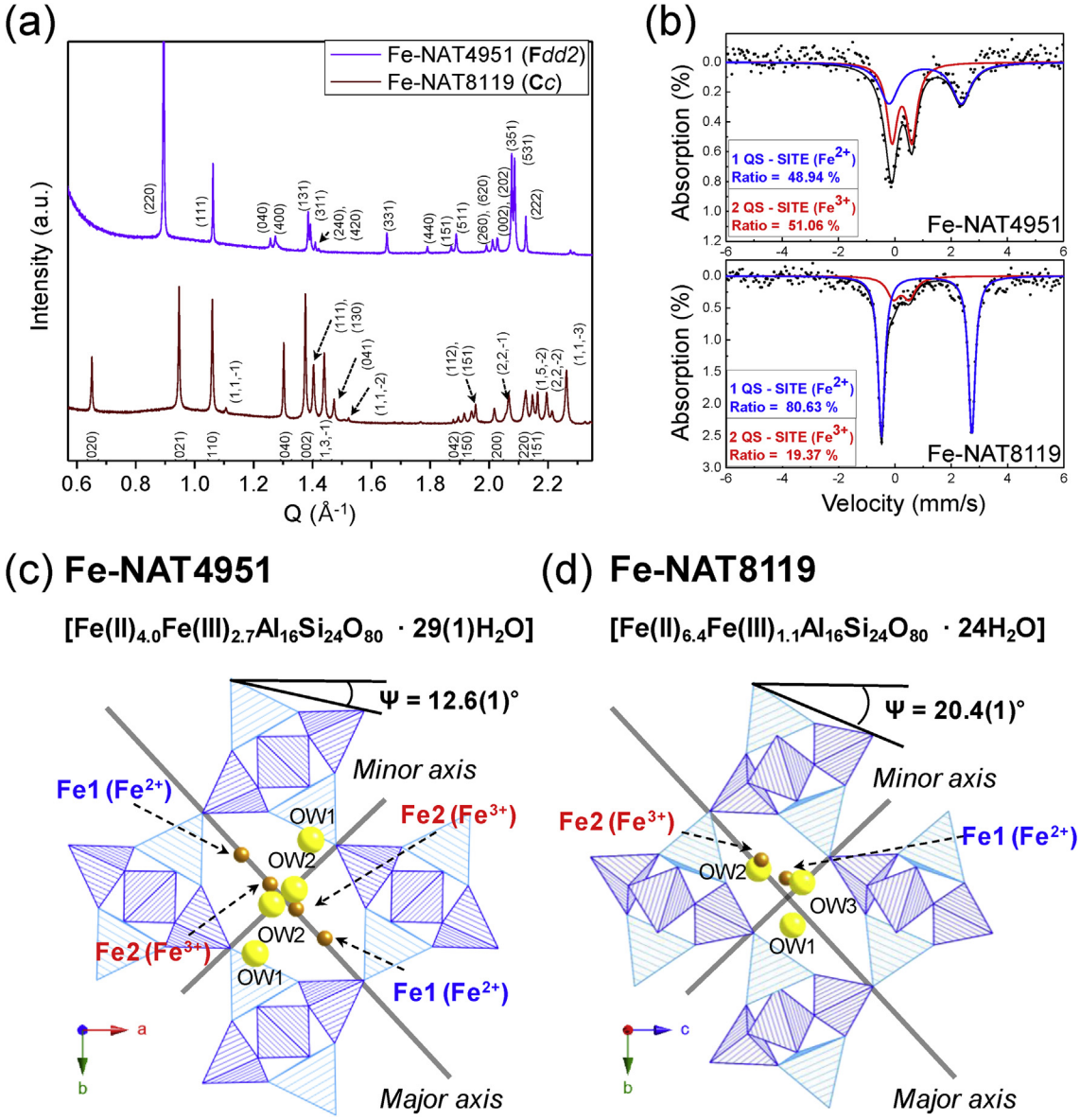

Fig. 1. (a) Synchrotron X-ray powder diffraction patterns of Fe-NAT4951 and Fe-NAT8119 with different $Fe^{2+/3+}$ ratios at ambient conditions. Miller indices of the Bragg reflections are shown. (b) Mössbauer spectra of Fe^{2+} and Fe^{3+} in Fe-NAT4951 and Fe-NAT8119. Polyhedral representations of (c) Fe-NAT4951 and (d) Fe-NAT8119. Striped sky (blue) tetrahedrons illustrate ordered distributions of Al (Si) atoms in the framework. Yellow balls are oxygen atoms of water molecules and ocher balls represent Fe^{2+} and Fe^{3+}cations. (For interpretation of the references to colour in this figure legend, the reader is referred to the web version of this article.)

Accelerator Laboratory (PAL). The incident X-rays were vertically collimated by a mirror, and monochromatized to obtain a wavelength of 1.5474(1) Å using a double-crystal Si (111) monochromator. The detector arm of the vertical scan diffractometer was composed of six sets of Soller slits, flat Ge (111) crystal analyzers, anti-scatter baffles, and scintillation detectors, with each set separated by 20° in 2θ. Each specimen of approximately 0.2 g powder was prepared using a flat plate side loading method to avoid preferred orientation. The sample was then rotated about the normal to the surface during the measurement, in order to improve the random powder sampling statistics. Step scans were performed at room temperature from 8° in 2θ with 0.005° increments and 2° overlaps of the detector bank, up to 128.5° in 2θ (Fig. 1a).

High-pressure synchrotron X-ray powder diffraction experiments were performed at the 9A beam line at PAL. The primary beam from an undulator was directed on a Si (111) crystal, and sets of parallel slits were used to create monochromatic X-rays with a wavelength of 0.6155(1) Å. The wavelength of the incident beam was determined using a LaB_6 standard (SRM 660b). A modified Merrill-Bassett diamond anvil cell (DAC) was used for the high-pressure experiments, equipped with type-I diamond anvils (culet diameter of 800 μm) and tungsten-carbide supports [23]. A stainless-steel foil of 250 μm thickness was pre-indented to a thickness of about 120 μm and holes with 400 μm diameters were obtained by electro-spark erosion. The powder sample was placed in the gasket hole together with some ruby chips for *in situ* pressure measurements. First, we collected ambient pressure data on the dry powder sample inside the DAC. Subsequently, we added water to the sample chamber as a hydrostatic pressure-transmitting medium [24], and the second ambient pressure data were taken-we refer to this as 'wet condition'. Subsequently, water was added again to the sample chamber and then the DAC was sealed to the first pressure point. The pressure of the sample in the DAC was measured by detecting the shift in the R1 emission line of the included ruby chips (precision: ± 0.05 GPa) [25]. The sample was typically equilibrated for about 10 min in the DAC at each measured pressure.

In situ high-temperature synchrotron X-ray powder diffraction experiments were performed at the 10C beam line at PAL. A beam from a multipole wiggler incident beams was vertically collimated by a collimating mirror (Rh-, Pt-coated 2 strips). Sets of parallel slits were used to create a 150 μm beam of monochromatic X-rays with wavelengths of 0.61992(1) Å. An image plate detector (Mar345, Mar Research, Germany) was used to collect data with a resolution of $\Delta d/d \sim 10^{-2}$ in an arrangement with a 300 mm sample to detector distance (2θ coverage up to ca. 43°) and 300 s exposure times. The powder samples were packed into 1.0 mm quartz capillaries connected to a vacuum to facilitate dehydration. The capillaries were then placed inside a heating coil [26]. The temperature was increased from ambient to 300 °C or 450 °C in 25 °C increments. A 2D charge coupled device (CCD) detector (Rayonix SX165, USA) was used to collect powder diffraction data at a resolution of $\Delta d/d \sim 10^{-4}$. The wavelength of the incident beam was determined using a LaB_6 standard (SRM 660b).

Pressure or temperature-dependent changes in the unit-cell lengths and volume were derived from a series of whole profile fitting procedures using the GSAS suite of programs [27]. The background was fixed at selected points, a pseudo-Voigt profile function proposed by Thompson et al. was used to model the observed Bragg peaks [28]. The structural models of the as-prepared phases (Fe-NAT4951 and Fe-NAT8119), high-pressure and high-temperature forms of the Fe-NATs were obtained by Rietveld refinements [27,29,30]. A March-Dollase function [31] was needed to account for preferred orientation. In order to reduce the number of parameters, isotropic displacement factors were refined by grouping the framework tetrahedral atoms, the framework oxygen atoms, and the non-framework cations, respectively. Geometrical soft-restraints on the T-O (T = Si, Al) and O–O bond distances of the tetrahedra were applied: the distances between Si–O and Al–O were restrained to values of 1.620 ± 0.001 Å and 1.750 ± 0.001 Å, respectively, the O–O distances were restrained to 2.646 ± 0.005 Å for the Si-tetrahedra and 2.858 ± 0.005 Å for the Al-tetrahedra. In the final stages of the refinements, the weights of the soft-restraints were gradually reduced. This did not lead to any significant changes in the interatomic distances, and convergence was achieved by simultaneously refining all background and profile parameters, scale factors, lattice constants, 2θ zero (fixed 2θ zero in all high-temperature models), preferred orientation function, and the atomic positional and thermal displacement parameters. The final refined parameters are summarized in Supporting Tables 1 and 3, and the selected bond distances and angles are listed in Supporting Tables 2 and 4.

3. Result and discussion

3.1. Characterization of as-prepared samples

To determine the ratio of Fe^{2+} to Fe^{3+} we used Mössbauer spectroscopy (see Fig. 1b). Following the procedure of Ovanesyan et al. [32,33] we extracted the Mössbauer doublets of Fe^{2+} and Fe^{3+} and their isomer shift (IS) and quadrupole splitting (QS) from the data (Fig. 1b and Table 1). The relative integrated areas for Fe^{2+} and Fe^{3+} signals in the Fe-NAT4951 are 49% and 51%. In Fe-NAT8119, the Fe^{2+} and Fe^{3+} spectral areas were 81% and 19%, respectively. Constrained by these Mössbauer experiments, the chemical compositions of Fe-NAT4951 and Fe-NAT8119 used in our Rietveld refinements lead to the following stoichiometries: $Fe^{2+}_{4.0}Fe^{3+}_{2.7}Al_{16}Si_{24}O_{80}\cdot 29(1)\ H_2O$ and $Fe^{2+}_{6.4}Fe^{3+}_{1.1}Al_{16}Si_{24}O_{80}\cdot 24(1)\ H_2O$. Residual amounts of the K^+ cation were not considered in our structural investigations. The different chemical compositions of the two samples are due to their different cation-exchange procedures. In an aqueous $FeCl_2\cdot 4H_2O$-solution the Fe^{2+} cation will readily oxidize to Fe^{3+} during the synthesis of Fe-NAT4951. Due the presence of more Fe^{3+} cations more vacancies will be present in the channels, which results in a higher H_2O content. The amount of Fe^{3+} and H_2O molecules in Fe-NAT2951 is therefore larger than in Fe-NAT8119. Compared to other exchanged

Table 1
Mossbauer results of Fe-NAT4951 and Fe-NAT8119 at room temperature.[a]

Sample name	Fe^{2+}			Fe^{3+}		
	Doublet 1 (blue)			Doublet 2 (red)		
	ΔE_Q (mm/s)	δ (mm/s)	Area (%)	ΔE_Q (mm/s)	δ (mm/s)	Area (%)
Fe-NAT4951	2.57	1.08	48.94	0.71	0.26	51.06
Fe-NAT8119	3.21	1.13	80.63	0.57	0.23	19.37

[a] Accompanied with Fig. 1b.

natrolites [12,14] Fe-NAT4951 contains the most H_2O molecules per 80 framework oxygens (O_f).

At ambient conditions, X-ray powder diffraction patterns (Fig. 1a) revealed that all Bragg reflection peaks observed in the Fe-NAT4951 sample could be indexed in an orthorhombic **F***dd2* space group, while the one observed from the Fe-NAT8119 sample were indexed in a monoclinic **C***c* space group. Rietveld refinements were done to characterize the structure in more detail. The Fe sites were found within the 8 ring channels aligned along the major axis (Fig. 1c and d). In the Fe-NAT4951, both Fe(1) and Fe(2) sites (Fe^{2+} and Fe^{3+}, respectively) respectively are occupied. Four water molecules, OW(1) and OW(2), are found approximately along the minor axis of the 8 ring. The OW(1) and OW(2) sites are in proximity to the framework and towards the middle of the channel, respectively. On the other hand, the Fe(1) and Fe(2) sites in Fe-NAT8119 are located in an asymmetrical way in the channel without being mirrored across the minor axis of the 8 ring. Three fully occupied water sites were located, two of them in close proximity to the Fe(1) and Fe(2) site. The Fe-NAT4951 shape of the channel is more circular than the one in Fe-NAT8119. The channel opening depends on the T_5O_{10} (T = Si,Al) chain rotation angle, Ψ, which (see Fig. 1c and d) were found to be 12.6(1)° and 20.4(1)° for the Fe-NAT4951 and Fe-NAT8119, respectively.

To further investigate the coordination around the Fe(1) and Fe(2) sites, Fe *K*-edge X-ray absorption data were measured. The EXAFS signal was extracted and the normalized χ(k) function was weighted by multiplying with k^3. The radial distribution functions are shown in Fig. 2a and b. Distances up to 3.0 Å are compared to the interatomic distances derived from the Rietveld models. To compare interatomic distances from the EXAFS analysis with those derived from Rietveld models we de-convoluted distances of the Fe-NAT4951 and Fe-NAT8119 within 3.0 Å and list them in Table 2. In Fe-NAT4951, interatomic distances based on EXAFS data were found at 1.8(2), 2.0(1), 2.45(6), 2.8(1) and 2.9(2) Å. The Rietveld refined model of the Fe-NAT4951 reveals that the Fe(1) site was coordinated by two H_2O and one framework oxygen O_f (Fig. 2c). The interatomic distances of the Fe(1) coordination sphere range from 2.52(9)Å to 2.85(7)Å. The Fe(2) site is coordinated by three H_2O molecules and one O_f, and the atomic distance range from 1.7(1)Å to 3.0(1)Å. On the other hand, the coordination sphere of Fe in Fe-NAT8119 is composed of distances at 1.8(2), 2.1(1), 2.26(7) and 2.8(2) Å. The Rietveld model of Fe-NAT8119, shows that the Fe(1) site is coordinated by three H_2O molecules and three O_f (Fig. 2d). The interatomic distances between Fe(1) and H_2O range from 1.80(3) to 2.18(4) Å whereas distances between Fe(1) and O_f range

Table 2
Comparison of de-convoluted distances from EXAFS and selected interatomic distances from Rietveld refinement.

de-convoluted distances	Distances from refinement			
	Fe(1), (2+)		Fe(2), (3+)	
Fe-NAT4951				
1.8(2)			Fe(2)–OW(2)	1.7(1)
2.0(1)			Fe(2)–OW(2)	1.94(9)
2.45(6)	Fe(1)–OW(2)	2.52(9)	Fe(2)–O(2)	2.6(2)
2.8(1)	Fe(1)–O(3)	2.82(8)		
	Fe(1)–OW(1)	2.85(7)		
2.9(2)			Fe(2)–OW(1)	3.0(1)
Fe-NAT8119				
1.8(2)	Fe(1)–OW(2)	1.80(3)	Fe(2)–OW(2)	1.8(1)
2.1(1)	Fe(1)–OW(1)	2.04(4)	Fe(2)–OW(3)	2.14(8)
	Fe(1)–O(2)	2.17(2)		
	Fe(1)–OW(3)	2.18(4)		
2.26(7)	Fe(1)–O(8)	2.43(2)		
	Fe(1)–O(1)	2.48(2)		
2.8(2)	Fe(1)–Al	2.87(2)	Fe(2)–O(8)	2.7(1)
			Fe(2)–O(10)	3.0(1)

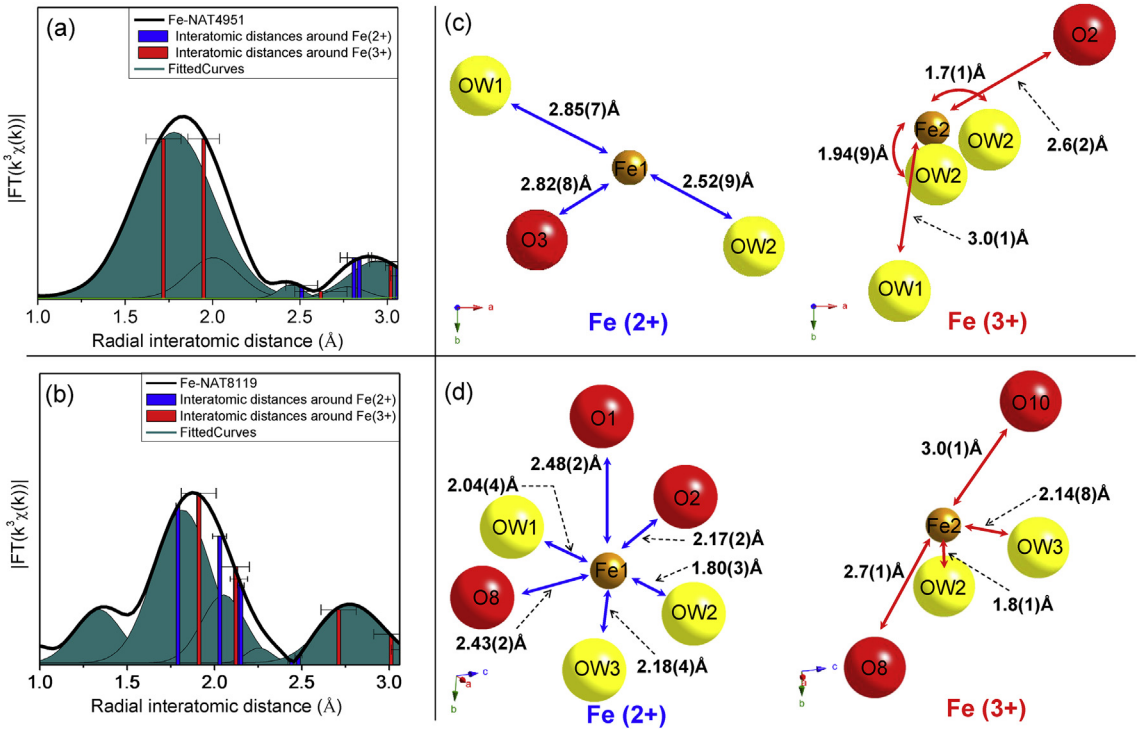

Fig. 2. The k^3 weighted Fourier transformation of Fe *K*-edge EXAFS of (a) Fe-NAT4951 and (b) Fe-NAT8119. Blue and red bars represent interatomic distances in the coordination of Fe^{2+} and Fe^{3+} derived from Rietveld refinement, respectively. Dark cyan peaks represent de-convoluted distances from EXAFS data. Refined coordination spheres and bond distances around Fe^{2+} and Fe^{3+} of (c) Fe-NAT4951 and (d) Fe-NAT8119. Yellow and red balls represent oxygens of H_2O molecules and frameworks, respectively. Ocher balls represent Fe^{2+} and Fe^{3+}cations. (For interpretation of the references to colour in this figure legend, the reader is referred to the web version of this article.)

from 2.17(2) to 2.48(2) Å. The coordination sphere around the Fe(2) site contain two H_2O molecules and two O_f. The interatomic distances between Fe(2) and H_2O range from 1.8(1) to 2.14(8) Å whereas the distances between Fe(2) and O_f are between 2.7(1) and 3.0(1) Å. Overall, the higher coordination numbers and shorter interatomic distances of Fe(1) and Fe(2) in Fe-NAT8119 compared to Fe-NAT4951 are a consequence of the more elliptical channel which brings more framework oxygen atoms into close enough proximity to coordinate to the Fe cations.

3.2. High-pressure experiments

Whole profile (LeBail) refinements reveal detailed unit cell parameter changes of the two Fe-NATs as a function of hydrostatic pressure as depicted in Figs. 3 and 4. In the Fe-NAT4951, all unit cell parameters slightly expand when they are under 'wet conditions' (see experimental part) and subsequently decrease linear with pressure. The unit cell volume increases by about 0.4(1) % under 'wet conditions'. In contrast, all unit cell parameters of Fe-NAT8119 abruptly increase near 1.0(1) GPa as a discontinuous pressure-induced hydration (PIH) [19] takes place and subsequently decrease linear with pressure. The unit cell volume increases by about 14.1(1) % during PIH. The volume of the recovered Fe-NAT4951 is similar to its volume at ambient conditions, whereas the volume of Fe-NAT8119 is 12.9(1) % larger after pressure release. The bulk modulus of Fe-NAT4951 is 78(4) GPa. The bulk moduli of Fe-NAT8119 before and after 1.0(1) GPa are 71(3) GPa and 36(1) GPa, respectively. According to previous high pressure studies of zeolites with T_5O_{10} units [18,19,34–43], the volume compressibility in this so-called "fibrous zeolite group" can be controlled by the type of extra-framework cations and water in the pores. We reported that the systematic compressibility of various cation forms of natrolites with comparable water content depend on the size and/or ionic potential of the EFCs [16,17]. In this study, the bulk modulus of Fe-NAT4951 is almost twice that of Fe-NAT8119 even though Fe-NAT4851 has a similar unit volume and, as shown below, even the same number of H_2O molecules near 1.0(1) GPa.

Rietveld refinements performed at different pressures allowed us to obtain more detailed structural models (Fig. 5). The Fe-NAT4951 is sensitive to humidity, and the sites of all H_2O molecules are fully occupied under 'wet conditions' as the chain rotation angle reduces to 12.3(1)°. The atomic positions of both Fe(1) and Fe(2) cations are similar to those established in the ambient structural model (Supporting Table 1). The coordination around Fe(1) is three (one bond with O_f and two bonds with H_2O molecules) whereas it is four around Fe(2) (one bond with O_f and three bonds with H_2O molecules) in the channel (Supporting Table 2). At a pressure of 3.5(1) GPa, the 8 ring channel becomes more elliptical as indicated by the larger rotational angle Ψ of 16.0(2)°. The coordination of Fe(1) changes to four (one bond with O_f and three bonds with H_2O molecules) whereas around Fe(2) it becomes three (one bond with O_f and two bonds with H_2O molecules). We suggest that these changes in coordination are due to Fe(1) and Fe(2) moving towards the center of the channel as the ellipticity of the 8 ring channel increases with pressure. The recovered model of Fe-NAT4951 looks similar to the ambient model with Ψ = 12.7(1)°

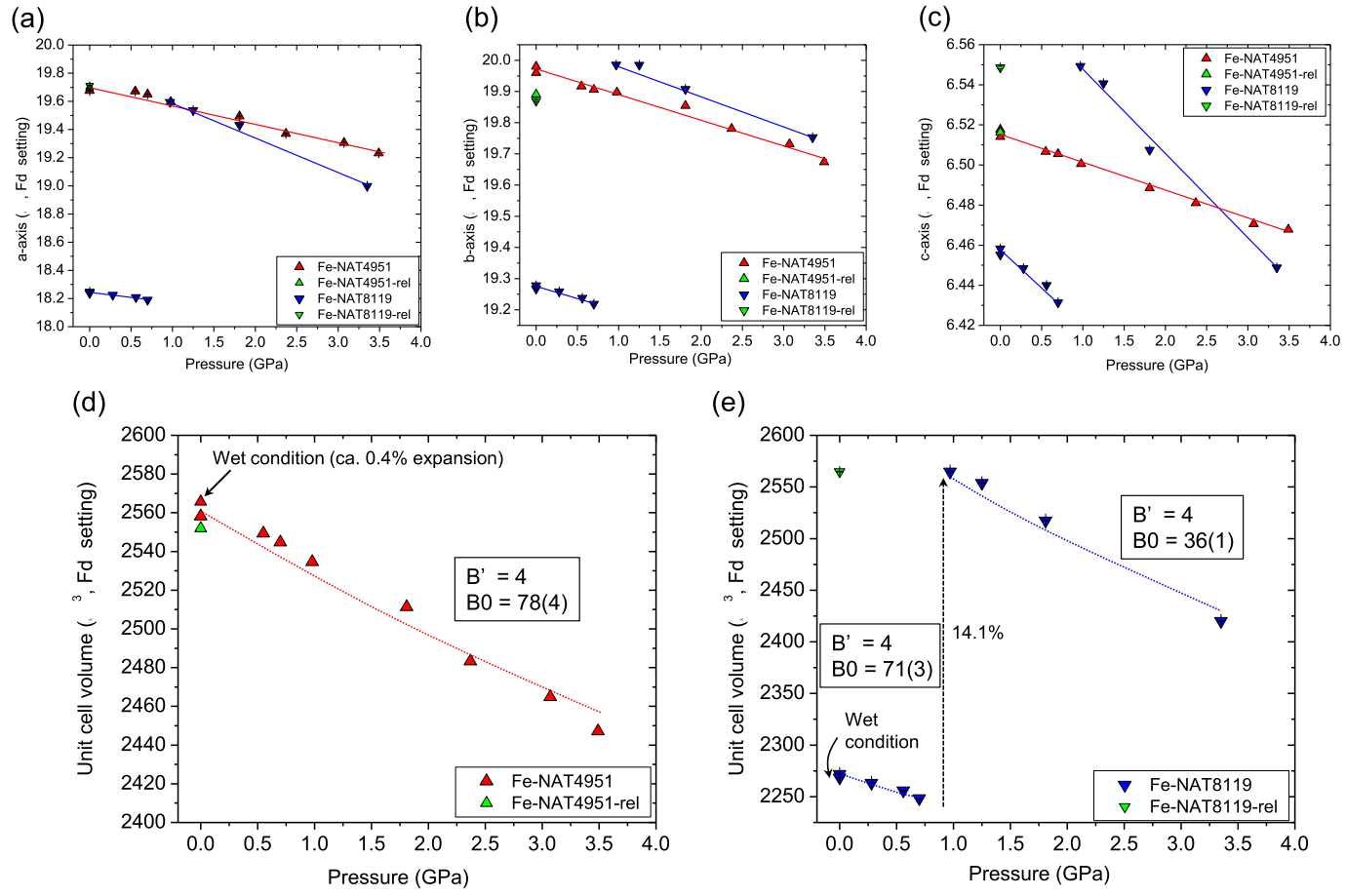

Fig. 3. Refined *a*-axis (a), *b*-axis (b), *c*-axis (c) and unit cell volume of Fe-NAT4951 (d) and Fe-NAT8119 (e) (red and blue symbols, respectively) as a function of pressure. Green symbols show parameters after pressure release. (For interpretation of the references to colour in this figure legend, the reader is referred to the web version of this article.)

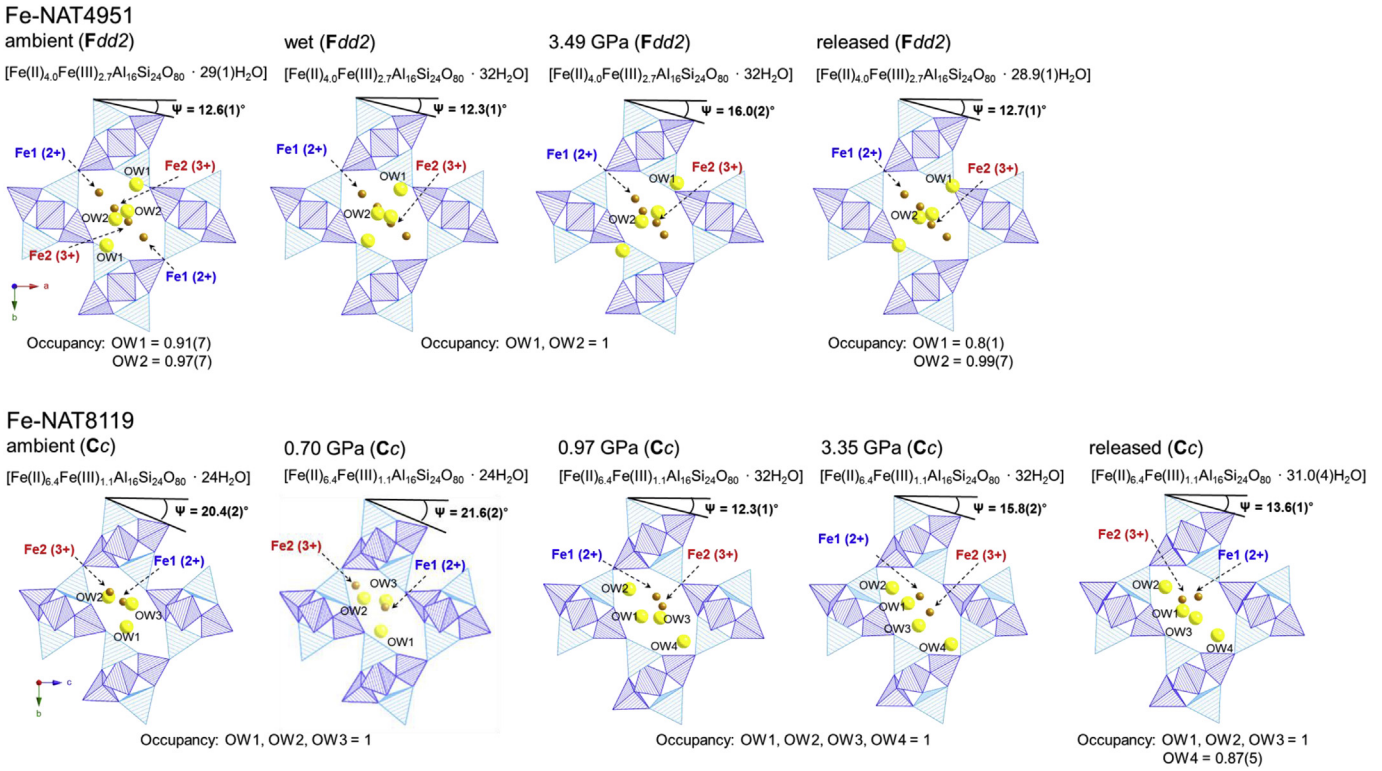

Fig. 4. Polyhedral representations of the structures of (a) Fe-NAT4951 and (b) Fe-NAT8119 at different pressures. Striped blue tetrahedrons illustrate ordered distributions of Al (Si) atoms in the framework. Yellow balls are oxygen of water molecules and ocher balls represent Fe^{2+} and Fe^{3+}cations. (For interpretation of the references to colour in this figure legend, the reader is referred to the web version of this article.)

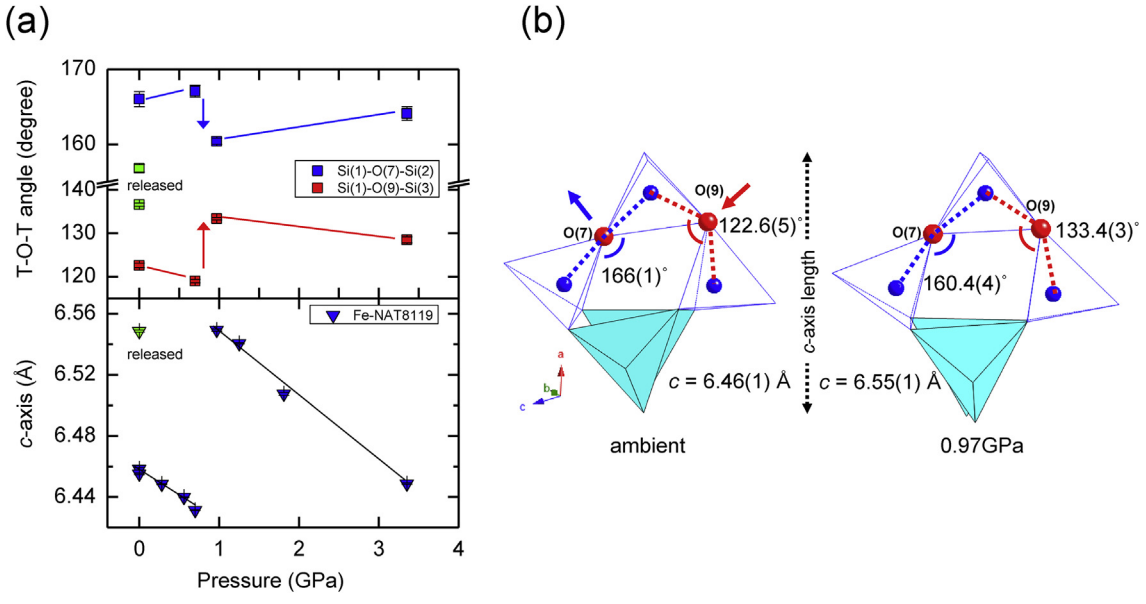

Fig. 5. (a) The *c*-axis and selected T-O-T angles in Fe-NAT8119. (b) Polyhedral representations of the natrolite secondary building unit of Fe-NAT8119 at ambient conditions and 0.97 (10) GPa. Blue balls and red balls are Si atoms and framework oxygens, respectively. (For interpretation of the references to colour in this figure legend, the reader is referred to the web version of this article.)

and the H_2O molecules now start to diffuse out of the channel. On the other hand, the structure of Fe-NAT8119 changes dramatically under pressure (Fig. 4b). Up to 0.7(1) GPa, the Fe(2) cation migrates towards the framework and away from the major axis. At ambient conditions the coordination number of the Fe(2) cation is three, with one coordination to O_f and two to H_2O molecules. At 0.7(1) GPa the coordination number increases to four, with now three to O_f and one to an H_2O molecule. Near 1.0(1) GPa, the OW(2) site pushes the Fe(2) cation to an adjacent channel due to a rearrangement of the H_2O molecules as pressure-induced hydration (PIH) occurs. Then a Fe(2) cation from a neighboring channel moves close to the Fe(1) site. At 1.0(1) GPa PIH leads to a decrease of the

chain rotation angle to 12.3(1)°. At 3.35(1) GPa Ψ increases back to 15.8(2)°. Both the migration of the Fe(2) cation and expansion of the NAT channel due to PIH reduces the coordination of Fe(2): from four-fold coordination at 0.7(1) GPa to two-fold coordination at 1.0(1) GPa. The Fe(2) cation migrates along the major axis under further pressure increase, and augments its coordination number to five at 3.35(1) GPa. After PIH at 1.0(1) GPa, the amount of H_2O molecules per 80 O_f increases from 24 to 32, a stoichiometry closer to the one found in Fe-NAT4951. After pressure release, the expanded channel remains (Ψ = 13.6(1)°) but the occupancy of OW(4) site decreases from full occupancy to 0.87(5).

In our previous high-pressure studies of natrolites, the *c*-axis showed contraction in contrast to the expanding *a*- and *b*-axes under pressure [16,17]. An expansion of the *c*-axis during PIH is observed in the Fe-NAT8119 sample. This is due to a highly distorted NAT framework, $\beta = 105.551(8)$, at ambient conditions. To compare with Ca-NAT (109.70(1)) or Sr-NAT (109.47(1)) [10] which also crystallize in the monoclinic **C***c* space group, the Fe-NAT8119 has a smaller β angle. The distortion in the Fe-NAT8119 structure manifests itself in the T-O-T angles which are the links capping adjacent SiO_4-tetrahedra in the NAT framework (Fig. 5b). Si(1)-O(7)-Si(2) and Si(1)-O(9)-Si(3) are 166(1)° and 122.6(5)° at ambient conditions, respectively. Under 1.0(1) GPa, the increase of the Si(1)-O(7)-Si(2) angle and the concomitant decrease of the Si(1)-O(9)-Si(3) angle monitors the growing strain in the natrolite framework under pressure (Fig. 5a). The Si(1)-O(7)-Si(2) angle then abruptly decreases to 160.4(4)° while concomitant the Si(1)-O(9)-Si(3) angle jumps to 133.4(3)° during PIH at 1.0(1) GPa and the *c*-axis parameter increases to 6.5493(7) Å. Upon further pressure and released pressure, the changes of the T-O-T angles are then coupled to those of the *c*-axis, as shown in Fig. 5a.

3.3. In-situ high-temperature experiments

Refined unit cell parameters of the two Fe-NAT samples as a function of temperature are plotted in Fig. 6. The unit cell of Fe-NAT4951 suddenly contracts at 125(1) °C and subsequently the peak intensities diminish, indicating a loss of crystallinity and the emergence of a disordered material (Supporting Fig. 2a). The recovered sample and the one measured at 300 °C show very similar broad peaks. The unit cell volume of Fe-NAT4951 contracts by about 8.3% at 125(1) °C. Until 125(1) °C the thermal expansion coefficient (α_{vol}) of this sample ranges from -1.3(2) x 10^{-4} °C^{-1} to -7.8(1) x 10^{-4} °C^{-1}. After 125(1) °C the coefficient changes between -1.4(1) x 10^{-3} °C^{-1} and -7.0(2) x 10^{-4} °C^{-1}. TGA data and Rietveld refinement-based structural models indicate that the partial thermal dehydration results in negative thermal expansion coefficients (Fig. 7a and Supporting Fig. 3a and b). At 225(25) °C, the Fe-NAT8119 phase transforms from a **C***c* (monoclinic) to a **F***dd2* (orthorhombic) one while the unit cell volume is reduced by about 5.0%. The α_{vol} below 225(5) °C is -3(3) x 10^{-6} °C^{-1}, quite a small value. The TGA data, however, show that the weight reduction of the Fe-NAT8119 sample due to the loss of H_2O molecules below 225(5) °C gradually decreases up to 92.5(5) wt. % (Supporting

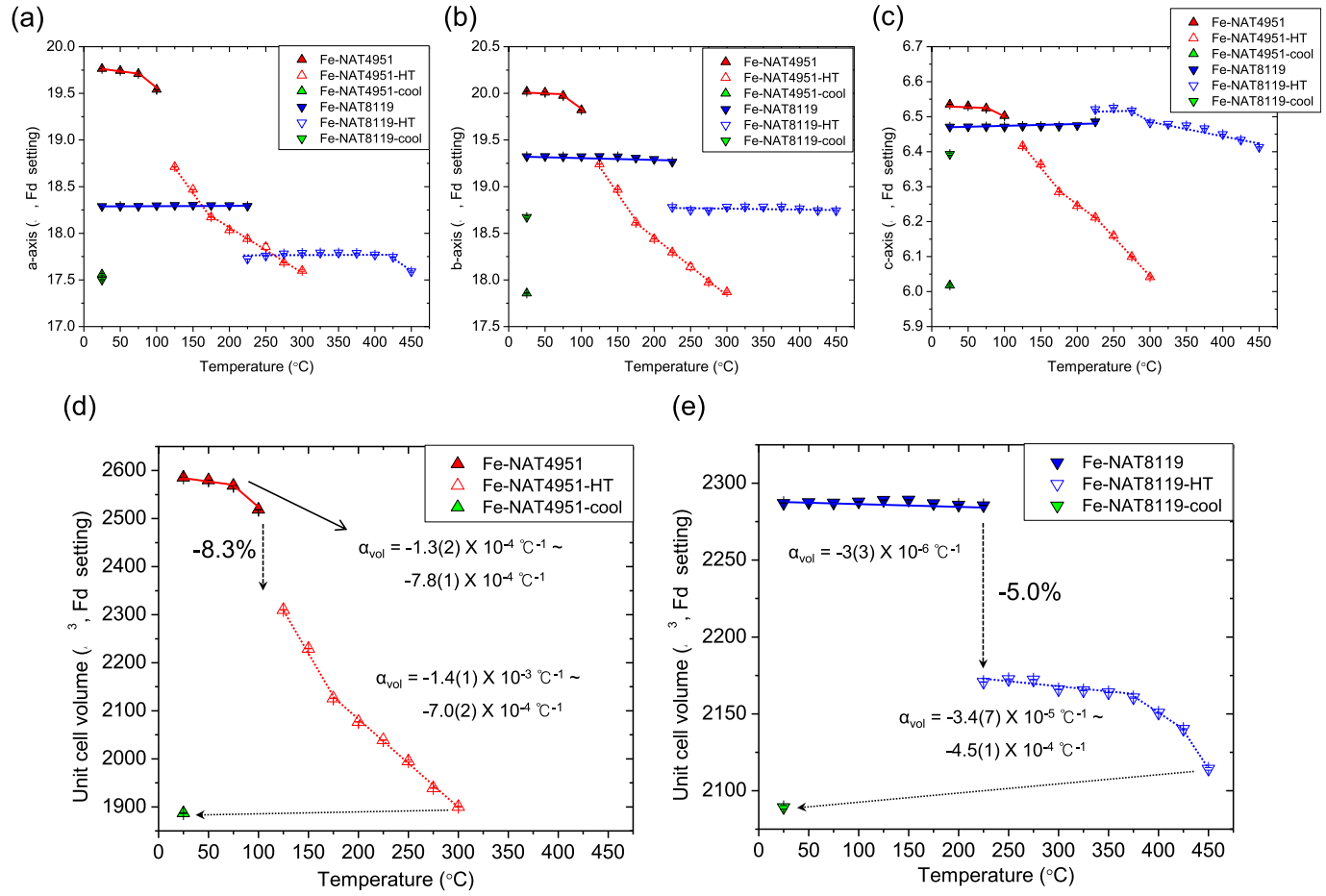

Fig. 6. Refined *a*-axis (a), *b*-axis (b), *c*-axis (c) and unit cell volume of Fe-NAT4951 (d) and Fe-NAT8119 (e) (red and blue symbols, respectively) as a function of temperature. Green symbols show parameters after cooling down to ambient temperature and exposing the samples for a week to ambient conditions. (For interpretation of the references to colour in this figure legend, the reader is referred to the web version of this article.)

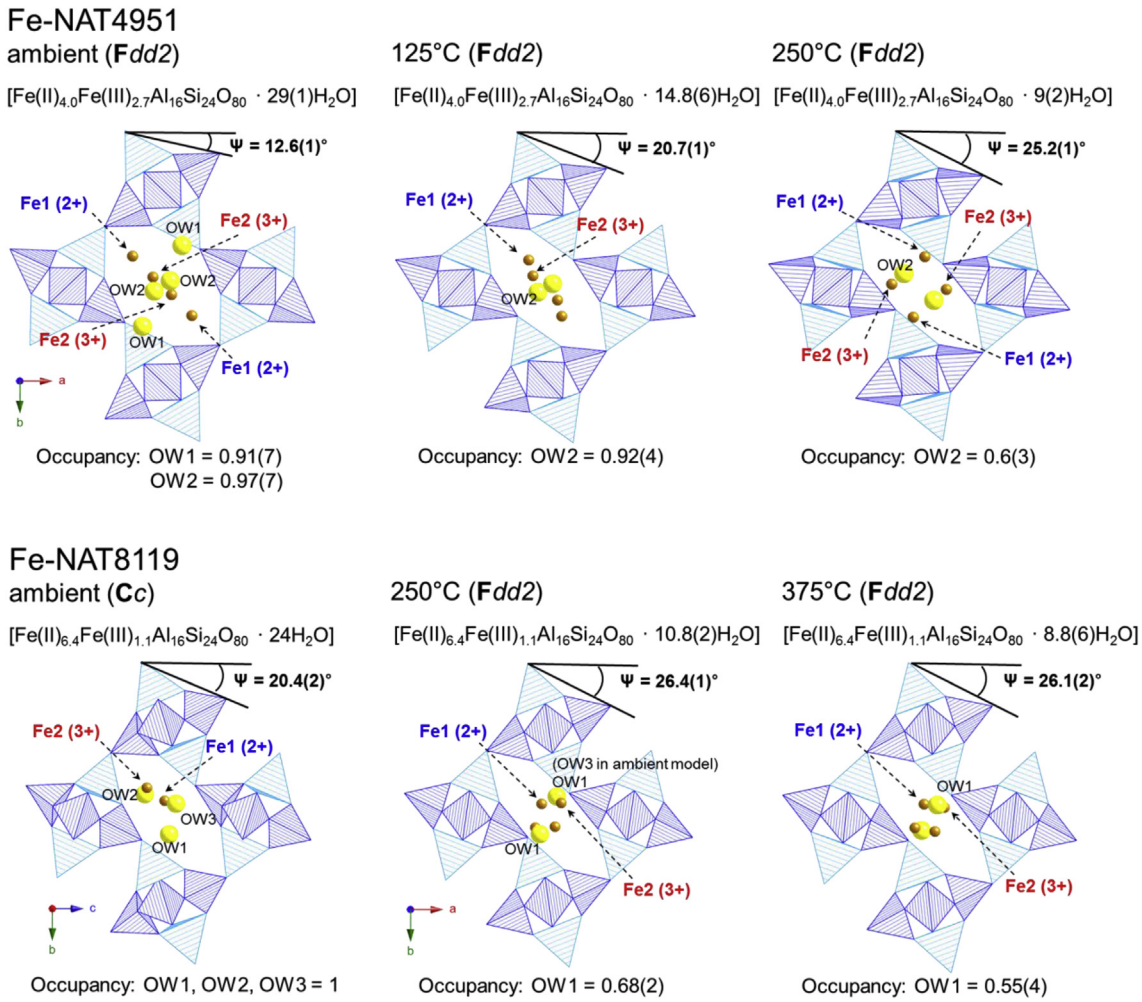

Fig. 7. Polyhedral structural representations of (a) Fe-NAT4951 and (b) Fe-NAT8119 at different temperatures. Striped blue tetrahedrons illustrate ordered distributions of Al (Si) atoms in the framework. Yellow balls are oxygen of water molecules and Ocher balls represent Fe^{2+} and Fe^{3+}cations. (For interpretation of the references to colour in this figure legend, the reader is referred to the web version of this article.)

Fig. 3b). We suspect that the volume contraction due to dehydration partially counteracts the thermal expansion of the Fe-NAT8119 framework. Above 225(5) °C, the thermal expansion coefficient changes from -3.4(7) x 10^{-5} °C^{-1} to -4.5(1) x 10^{-4} °C^{-1}. These increasing negative values corroborate that the loss of H_2O molecules becomes dominant after 225(5) °C.

Rietveld models of the Fe-NATs at selected temperatures are shown in Fig. 7. In Fe-NAT4951, the H_2O molecule in the OW(1) site initially dehydrates at 125(1) °C because of being only coordinated to two Fe cations. This is in contrast to OW(2) which is three-coordinated, and the distances between OW(1) and Fe cations are larger (2.6(2) Å - 2.85(7) Å) than those of the OW(2) site (1.7(1) Å - 2.52(9) Å). As a consequence of this partial dehydration of the OW(1) site, the number of H_2O molecules per 80 O_f decreases from 29(1) to 14.8(6). Furthermore, the channel becomes more elliptical ($\Psi = 20.7(1)°$) and the Fe cations migrate towards the middle of the channel. The H_2O molecules located in the OW(2) site begin to dehydrate from 125(1) °C on, and only 9(2) H_2O molecules remain in the channel at 250(5) °C. The Fe(1) and Fe(2) cations migrate by 1.17(1) Å and 1.93(1) Å towards an AlO_4 and SiO_4 tetrahedron, respectively. The OW(2) site splits apart by about 1.72(1) Å along the major axis of the channel. The chain rotation angle increases to 25.2(1)° after dehydration. On the other hand, the OW(2) site in the Fe-NAT8119 structure completely loses it H_2O molecules at 250(5) °C. The amount of H_2O molecules per 80 O_f decreases from 24 to 10.8(2). The other H_2O molecules located in OW(1) and OW(3), subsequently move towards the framework wall along the minor axis. Both Fe(1) and Fe(2) sites are separated, and Fe(1) and Fe(2) are located near the middle of the channel and in proximity to OW(1), respectively. The channel becomes more elliptical as indicated by a Ψ of 26.4(1)°. The refined model at 375(10) °C looks similar to the structure observed at 250(5) °C, though the amount of H_2O molecules decreases to 8.8(6) per 80 O_f. The chain rotation angle marginally decreases to 26.1(2)° at 375(10) °C.

In our previous high-temperature studies of natrolites [13,15], we argued that the framework at high temperature remains intact due to the bonding between the EFC and two bridging oxygens, i.e. O(2)-EFC-O(2). In this study, both the Fe(1) and Fe(2) site in the Fe-NAT4951 material do not have such an O(2)-EFC-O(2) bonding interaction at 125(1) °C and 250(5) °C. The structure of the Fe-NAT4951 therefore starts to collapse near 125(1) °C. However, in the Fe-NAT8119 the Fe(1) and Fe(2) have O(2)-Fe(1)-O(2) or O(2)-Fe(2)-O(2) bonding interactions up to 375(10) °C. Overall, the structure of the Fe-NAT8119 is therefore more stable at higher temperatures.

In both Fe-NAT samples the unit cell volume is strongly dependent on the T-O(2)-T angles and the ionic potential of the Fe cations at ambient and non-ambient conditions (Fig. 8). At ambient

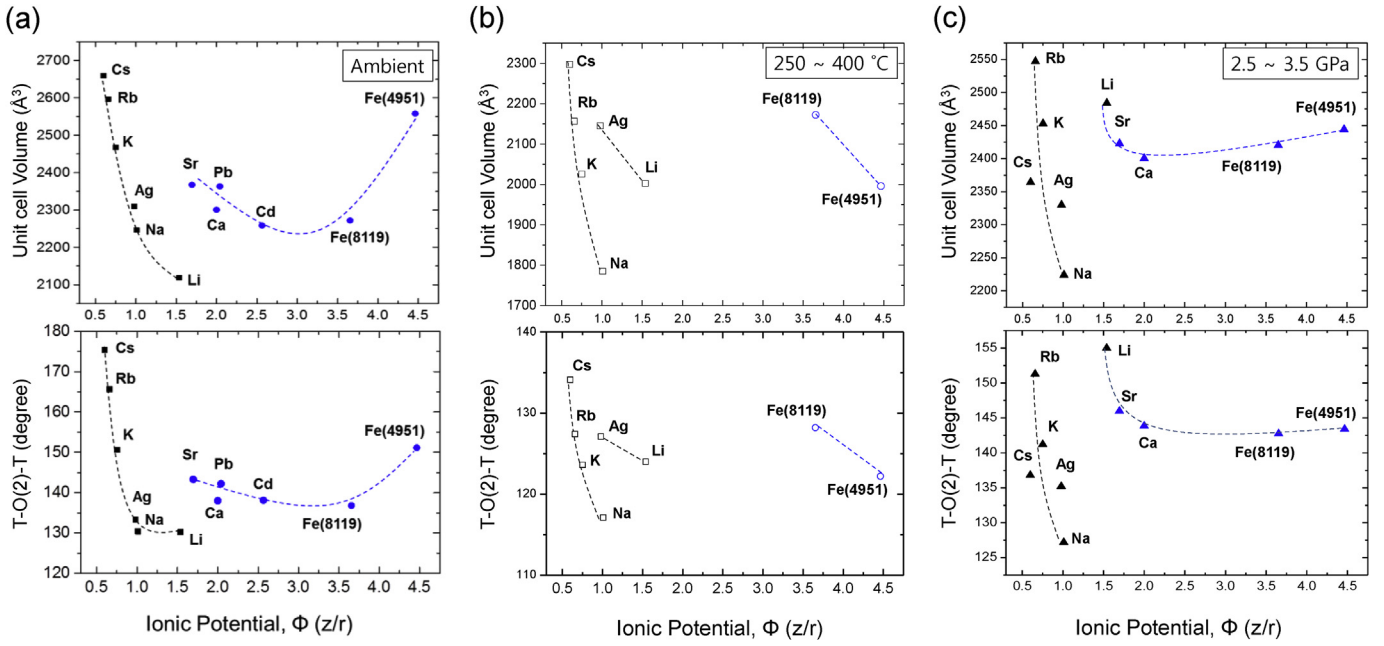

Fig. 8. Volume and T-O(bridging oxygen)-T angles of natrolites with different extra framework cations as a function of their ionic potential at (a) ambient conditions, (b) at elevated temperatures (250–400 °C) and (c) under hydrostatic pressure (2.5–3.5 GPa).

conditions, the volumes and T-O(2)-T angles of natrolites with monovalent EFC decrease as a function of the ionic potential. This angle varies from being almost linear in Cs-NAT at 175.4(4) ° to 130.7(4) ° in Li-NAT. In natrolites containing divalent and trivalent cations, the unit cell volumes and T-O(2)-T angles seem to follow an almost quadratic temperature-dependency. From Sr-NAT to Cd-NAT, volumes and angles decrease as a function of the ionic potential. At high-temperatures (250 °C ~ 400 °C), the unit cell volumes and T-O(2)-T angles of natrolites with monovalent EFC decrease as a function of their ionic potential. Both Li- and Ag-NAT have a unique temperature dependence due to channel reorientations taking place after dehydration [44]. The volumes and angles of Fe-NATs decrease as a function of the ionic potential. Under pressure (2.5 GPa ~3.5 GPa), the natrolite framework gradually contracts as a function of the ionic potential of the EFC.

4. Conclusion

In this study, we demonstrated that the structural properties of Fe-NATs at ambient and non-ambient conditions are closely related to the distributions of Fe^{2+} and Fe^{3+}cations. Chemical compositions of the as-prepared samples, Fe-NAT4951 and Fe-NAT8119, have different Fe^{2+} to Fe^{3+} ratios, namely $Fe^{2+}_{4.0}Fe^{3+}_{2.7}Al_{16}Si_{24}O_{80}\cdot 29(1)H_2O$ and $Fe^{2+}_{6.4}Fe^{3+}_{1.1}Al_{16}Si_{24}O_{80}\cdot 24H_2O$, respectively. At ambient conditions, the channels in Fe-NAT4951 are more circular with smaller chain rotation angles than those in Fe-NAT8119. Since Fe-NAT4951 contains more Fe^{3+} cations it creates more vacancies to coordinate H_2O molecules. Accordingly, Fe-NAT8119 undergoes a discontinuous PIH with volume expansion by ca. 14.1% near 1.0(1) GPa to increase its channel water content close to 32 H_2O, whereas Fe-NAT4951 contracts gradually under pressure from the fully hydrated state with 32 H_2O under wet conditions. The observed temperature-dependent structural changes are also different in the two samples as indicated by the different degrees of initial volume contraction and onset temperature of dehydration. Overall, Fe-NAT8119 appears to be more thermally stable than Fe-NAT4951 due to the presence of O(2)-Fe(1)-O(2) or O(2)-Fe(2)-O(2) bonding interactions at high temperatures.

In view of the recognized importance of Fe-containing zeolites [1–5] these structural investigations of two natrolites containing different ratios of Fe^{2+} and Fe^{3+} cations could become the basis for theoretical and experimental explorations of new heterogeneous catalysts at ambient and non-ambient conditions.

Acknowledgment

This work was supported by the Global Research Laboratory (NRF-2009-00408) and National Research Laboratory (NRF-2015R1A2A1A01007227) Programs of the Korean Ministry of Science, ICT and Planning (MSIP). We also thank the support of the NRF grants 2016K1A4A3914691 and 2016K1A3A7A09005244. Experiments using X-ray synchrotron radiation were supported by Pohang Accelerator Laboratory (PAL).

Appendix A. Supplementary data

Supplementary data related to this article can be found at http://dx.doi.org/10.1016/j.micromeso.2017.02.062.

References

[1] J.R. Anderson, P. Tsai, Chem. Commun. 19 (1987) 1435–1436.
[2] X. Feng, W. Keith Hall, J. Catal. 166 (1997) 368–376.
[3] G.I. Panov, V.I. Sobolev, K.A. Dubkov, A.S. Kharitonov, 1996, 493–502.
[4] V.I. Sobolev, G.I. Panov, A.S. Kharitonov, V.N. Romannikov, A.M. Volodin, K.G. Ione, J. Catal. 139 (1993) 435–443.
[5] T.V. Voskoboinikov, H.-Y. Chen, W.M.H. Sachtler, Appl. Catal. B Environ. 19 (1998) 279–287.
[6] George A. Olah, Alain Goeppert, G.K.S. Prakash, Beyond Oil and Gas: the Methanol Economy, Wiley-VCH Verlag GmbH & Co. KGaA, Weinheim, 2006.
[7] K. Lázár, A.N. Kotasthane, P. Fejes, Catal. Lett. 57 (1999) 171–177.
[8] G.I. Panov, A.K. Uriarte, M.A. Rodkin, V.I. Sobolev, Catal. Today 41 (1998) 365–385.
[9] L. Shu, J.C. Nesheim, K. Kauffmann, E. Münck, J.D. Lipscomb, L. Que Jr., Science 275 (1997) 515–518.

[10] B.E.R. Snyder, P. Vanelderen, M.L. Bols, S.D. Hallaert, L.H. Böttger, L. Ungur, K. Pierloot, R.A. Schoonheydt, B.F. Sels, E.I. Solomon, Nature 536 (2016) 317–321.
[11] B.L. Vallee, R.J. Williams, P. Natl. Acad. Sci. U. S. A. 59 (1968) 498–505.
[12] Y. Lee, Y. Lee, D. Seoung, Am. Mineral. 95 (2010) 1636–1641.
[13] Y. Lee, D. Seoung, Y.N. Jang, J. Bai, Y. Lee, Am. Mineral. 96 (2011) 1308–1315.
[14] Y. Lee, D. Seoung, Y. Lee, Am. Mineral. 96 (2011) 1718–1724.
[15] Y. Lee, D. Seoung, D. Liu, M.B. Park, S.B. Hong, H. Chen, J. Bai, C.-C. Kao, T. Vogt, Y. Lee, Am. Mineral. 96 (2011) 393–401.
[16] D. Seoung, Y. Lee, C.C. Kao, T. Vogt, Y. Lee, Chem. Eur. J. 19 (2013) 10876–10883.
[17] D. Seoung, Y. Lee, C.-C. Kao, T. Vogt, Y. Lee, Chem. Mater. 27 (2015) 3874–3880.
[18] Y. Lee, T. Vogt, J.A. Hriljac, J.B. Parise, G. Artioli, J. Am. Chem. Soc. 124 (2002) 5466–5475.
[19] Y. Lee, T. Vogt, J.A. Hriljac, J.B. Parise, J.C. Hanson, S.J. Kim, Nature 420 (2002) 485–489.
[20] Y. Lee, D. Seoung, Y.N. Jang, T. Vogt, Y. Lee, Chem. Eur. J. 19 (2013) 5806–5811.
[21] Y. Lee, J.A. Hriljac, T. Vogt, J. Phys, Chem. C 114 (2010) 6922–6927.
[22] D. Seoung, Y. Lee, H. Cynn, C. Park, K.-Y. Choi, D.A. Blom, W.J. Evans, C.-C. Kao, T. Vogt, Y. Lee, Nat. Chem. 6 (2014) 835–839.
[23] H.-K. Mao, R.J. Hemley, Philos. Trans. Roy. Soc. A 354 (1996) 1315–1332.
[24] S. You, D. Kunz, M. Stöter, H. Kalo, B. Putz, J. Breu, A.V. Talyzin, Angew. Chem. Int. Ed. 125 (2013) 3983–3987.
[25] P.M. Bell, H.K. Mao, in: Carnegie Inst. Washington Year Book, vol. 78, 1979, pp. 665–669.
[26] K. Stahl, J. Hanson, J. Appl. Crystallogr. 27 (1994) 543–550.
[27] B.H. Toby, J. Appl. Crystallogr. 34 (2001) 210–213.
[28] P. Thompson, D.E. Cox, J.B. Hastings, J. Appl. Crystallogr. 20 (1987) 79–83.
[29] A.C. Larson, R.B. VonDreele, Rep. LAUR (1986) 86–748.
[30] H.M. Rietveld, J. Appl. Crystallogr. 2 (1969) 65–71.
[31] W.A. Dollase, J. Appl. Crystallogr. 19 (1986) 267–272.
[32] N.S. Ovanesyan, K.A. Dubkov, A.A. Pyalling, A.A. Shteinman, J. Radioanal. Nucl. Ch. 246 (2000) 149–152.
[33] N.S. Ovanesyan, A.A. Shteinman, K.A. Dubkov, V.I. Sobolev, G.I. Panov, Kinet. Catal. 39 (1998) 792–797.
[34] P. Ballone, S. Quartieri, A. Sani, G. Vezzalini, Am. Mineral. 87 (2002) 1194–1206.
[35] M. Colligan, Y. Lee, T. Vogt, A.J. Celestian, J.B. Parise, W.G. Marshall, J.A. Hriljac, J. Phys. Chem. B 109 (2005) 18223–18225.
[36] P. Comodi, G.D. Gatta, P.F. Zanazzi, Eur. J. Mineral. 14 (2002) 567–574.
[37] D.G. Gatta, B.T. Ballaran, P. Comodi, F.P. Zanazzi, Phys. Chem. Min. 31 (2004) 288–298.
[38] D.G. Gatta, A.S. Wells, Phys. Chem. Min. 31 (2004) 465–474.
[39] G.D. Gatta, T.B. Ballaran, P. ComodI, P.F. Zanazzi, Am. Mineral. 89 (2004) 633–639.
[40] Y. Lee, A.J. Hriljac, A. Studer, T. Vogt, Phys. Chem. Min. 31 (2004) 22–27.
[41] Y. Lee, J.A. Hriljac, J.B. Parise, T. Vogt, Am. Mineral. 90 (2005) 252–257.
[42] A. Likhacheva, Y. Seryotkin, A. Manakov, S. Goryainov, A. Ancharov, M. Sheromov, High Press. Res. 26 (2006) 449–453.
[43] A.Y. Likhacheva, Y.V. Seryotkin, A.Y. Manakov, S.V. Goryainov, A.I. Ancharov, M.A. Sheromov, Am. Mineral. 92 (2007) 1610–1615.
[44] Y. Lee, D. Ahn, T. Vogt, Y. Lee, Am. Mineral., (submitted for publication).